

Quantitative modeling, optimization, and verification of ^{63}Ni -powered betavoltaic cells based on three-dimensional ZnO nanorod arrays

Zan Ding^{1, 2}, Tong-Xin Jiang^{1, 2}, Ren-Rong Zheng^{1, 2}, Na Wang^{1, 2}, Li-Feng Zhang³, Shi-Chao Liu⁴, Xin Li³, **, Hai-Sheng San (<https://orcid.org/0000-0002-6019-923X>)^{1, 2, *}

¹ Pen-Tung Sah Institute of Micro-Nano Science and Technology, Xiamen University, Xiamen 361005, China

² Shenzhen Research Institute of Xiamen University, Shenzhen 518000, China

³ China Institute of Atomic Energy, Beijing 102413, China

⁴ Shanghai Institute of Space Power-Sources, Shanghai 200245, China

*; ** Corresponding authors, sanhs@xmu.edu.cn (H. S. San); lixin_0128@sina.com (X. Li)

This study was supported by the National Natural Science Foundation of China (No. 12175190), the Special Funds for Central Government Guiding Shenzhen Development in Science and Technology (No. 2021Szvup066) and the Natural Science Foundation of Fujian Province, China (No.2022J02006).

Abstract

Betavoltaic cells (BCs) are promising self-generating power cells with long life and high power density. However, the low energy conversion efficiency (*ECE*) has limitations in practical engineering applications. Wide-bandgap semiconductors (WBGSS) with three-dimensional (3-D) nanostructures are ideal candidates for increasing the *ECE* of BCs. This paper proposes hydrothermally-grown ZnO nanorod arrays (ZNRAs) for ^{63}Ni -powered BCs. A quantitative model was established for simulation using the parameter values of the dark characteristics, which were obtained from the experimental measurements for a simulated BC based on a Ni-incorporated ZNRAs structure. Monte Carlo (MC) modeling and simulation were conducted to obtain the values of the β energy deposited in ZNRAs with different nanorod spacings and heights. Through the simulation and optimization of the 3-D ZNRAs and 2-D ZnO bulk structures, the performance of the ^{63}Ni -powered BCs based on both structures was evaluated using a quantitative model. The BCs based on the 3-D ZNRAs

structure and 2-D ZnO bulk structure achieved a maximum *ECE* of 10.1% and 4.69%, respectively, which indicates the significant superiority of 3-D nanostructured WBGSSs in terms of increasing the *ECE* of BCs.

Keywords: Betavoltaic cells; Monte Carlo simulation; ZnO nanorod arrays; Quantitative model; Performance evaluation.

1. Introduction

With the rapid development of wireless sensing networks for harsh environments (deep sea, deep ground, deep space, and polar and desert regions), the demand for micropower sources has increased significantly. Compared with conventional cells (chemical cells, fuel cells, and solar cells), betavoltaic cells (BCs) with longer lifetimes, stronger environment adaptiveness, and higher energy density have good application prospects and remarkable market potential [1].

Recently, reviews on BCs were published by Olsen et al. [2], Prelas et al. [3], and Spencer et al. [4]. According to Olsen's calculation model, the possible efficiency cap can reach as high as 35% for BCs employing wide-bandgap semiconductors (WBGs). However, the recorded energy conversion efficiency (ECE) reported for experimental betavoltaics is far less than 35% when using the available WBGs. In previous decades, research on BCs has received more attention, and related experimental studies have recorded the *ECE* in the order of 6% when using available WBGs (4H-SiC and diamond) [5–9]. To increase the output power (P_{out}) of BCs, multiple BCs are stacked modularly to generate microwatt-level output power [10]. However, the issue of low *ECE* has not been resolved to facilitate the practical engineering applications of BCs. It is expected that the loading and utilization efficiency of radioactive sources in energy conversion structures (ECSs) can be further improved using new strategies.

It is well understood that an ECS with a larger specific surface area can load more radioactive sources, which means that BCs can generate higher output power. In conventional planar diode structures, the *ECE* and output power density are limited owing to the low active area in the planar structure. In contrast, three-dimensional (3-D) nanostructures with a larger specific surface area can significantly increase the β energy conversion, which can be explained by the following four basic facts: i) the filling of radioisotope material into the interspace of 3-D nanostructures results in significant increase in the loading amount of radioisotope materials; ii) the combination of a radioisotope source with 3-D nanostructures results in the interaction of β particles with nanostructured ECSs in all directions, and thus the collection efficiency of the β particles dramatically increases; iii) the self-shielding effects of

the radioisotope source are cancelled owing to the nanometer-level thickness of the radioactive structure; iv) the effective junction region area of the 3-D nanostructure is significantly extended.

Recently, several evaluation studies considering a 3-D nanostructure have been conducted based on theoretical analysis or experimental verification. For example, Sun et al. [11] developed a BC based on a 3-D porous silicon *p-n* diode structure loaded with tritium gas, and achieved an *ECE* of 0.22%, which was ten times larger compared with that of a 2-D planar diode structure. Murphy et al. [12] designed a BC based on 3-D silicon diode structure incorporated with ¹⁴⁷Pm source, which achieved an *ECE* of 5.8% and power density of 25 mW/cm³. In our previous studies, WBGS TiO₂ (bandgap = 3.2 eV) and ZnO (bandgap = 3.37 eV) nanostructures were used to fabricate the ECSs of BCs [13–19]. A cost-effective anodic oxidation method and a hydrothermal method were used to prepare highly ordered and free-standing nanotube and nanorod array structures, respectively. Using a Nickel-63 (⁶³Ni) sheet as the radioisotope source and electrode, an enhanced betavoltaic effect was observed in the BCs. In the last decade, 3-D ZnO nanorod arrays (ZNRAs) have attracted extensive attention owing to their large bandgaps, high aspect ratios, and large specific surface areas. Compared with TiO₂, ZnO has longer electron lifetime and higher electron mobility [20], which is considered as one of the most promising electrode materials for photoelectronic devices. For example, in photodetectors using ZNRAs as the photoelectrodes, electrons can be rapidly transported along ZnO nanorods, which helps in suppressing the recombination of electron-hole pairs (EHPs) [21]. Additionally, ZNRAs can be synthesized on a wide variety of substrates for versatile electrode preparation [22]. However, devices based on pure ZNRAs are subjected to high carrier recombination owing to the lack of an effective separation mechanism for the EHPs. For BCs using ZNRAs, an effective method is to incorporate a metal-based radioactive material, such as ⁶³Ni or ¹⁴⁷Pm, into the interspaces of ZNRAs to form a core-shell structure with a Schottky junction that can considerably separate the EHPs. Additionally, the loading amount of the radiation source can be increased significantly compared with using ⁶³Ni sheets as the radiation source, which is conducive to increasing the *P_{out}* of BCs.

Recent studies on the optimal design of BCs with 2-D bulk structures have shown that

the size and structure of ECSs and the thickness of the radioactive source have significant influence on the performance of BCs [23–29]. However, few studies have been conducted on the influence of 3-D nanostructured ECSs combined with radioactive sources on the performance of BCs. Therefore, an accurate theoretical model must be established to evaluate the performance of BCs based on 3-D nanostructured WBGSSs.

This paper proposes a theoretical model for evaluating the performance of BCs based on 3-D nanostructured WBGSSs. A freestanding ZNRAs structure combined with normal Ni was used to simulate the ECSs to obtain the parameters of the dark characteristics. A Monte Carlo (MC) model based on the MCNP code was established to investigate the interaction between incident β particles and the ECSs. By combining the theoretical model with experimental data, the BCs based on the ^{63}Ni -incorporated ZNRAs structure can be accurately evaluated and further optimized.

2. Theory, design and experiment

2.1. MC simulation for β energy deposition on 3-D nanostructure

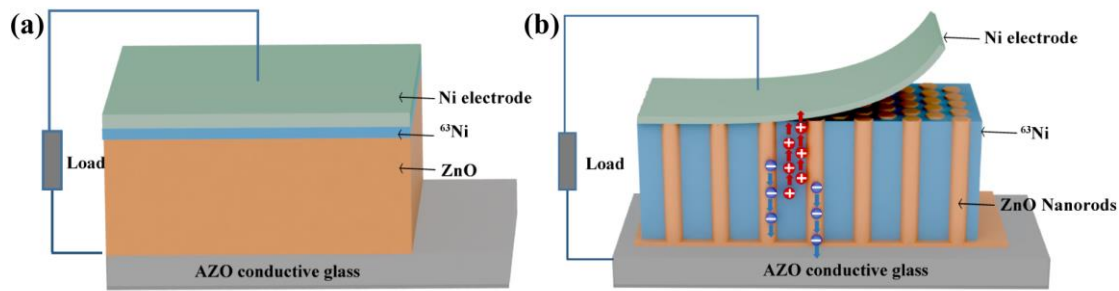


Fig. 1. (Color online) Schematic diagram of BCs based on (a) 2-D ZnO bulk structure and (b) 3-D ZNRAs structure.

To design an optimal structure of BCs, MC simulation [30] was conducted to investigate the interaction of β radiation with 3-D ^{63}Ni -incorporated ZNRA structures. As the β -emitting source, this study selected ^{63}Ni with a half-life of approximately 100 years, average energy of 17.4 keV, and maximum energy of 66 keV. Two types of BCs were designed to compare the energy deposition simulations. As shown in Fig. 1a, a sandwich-type BC based on a 2-D ZnO bulk structure consisted of an Al-doped ZnO (AZO)/glass substrate, ZnO film, and $^{63}\text{Ni}/\text{Ni}$ layer deposited on the ZnO film. In contrast, the 3-D nanostructured BC consisted of an

AZO/glass substrate, 3-D ZNRAs combined with ^{63}Ni , and a top Ni electrode (Fig. 1b).

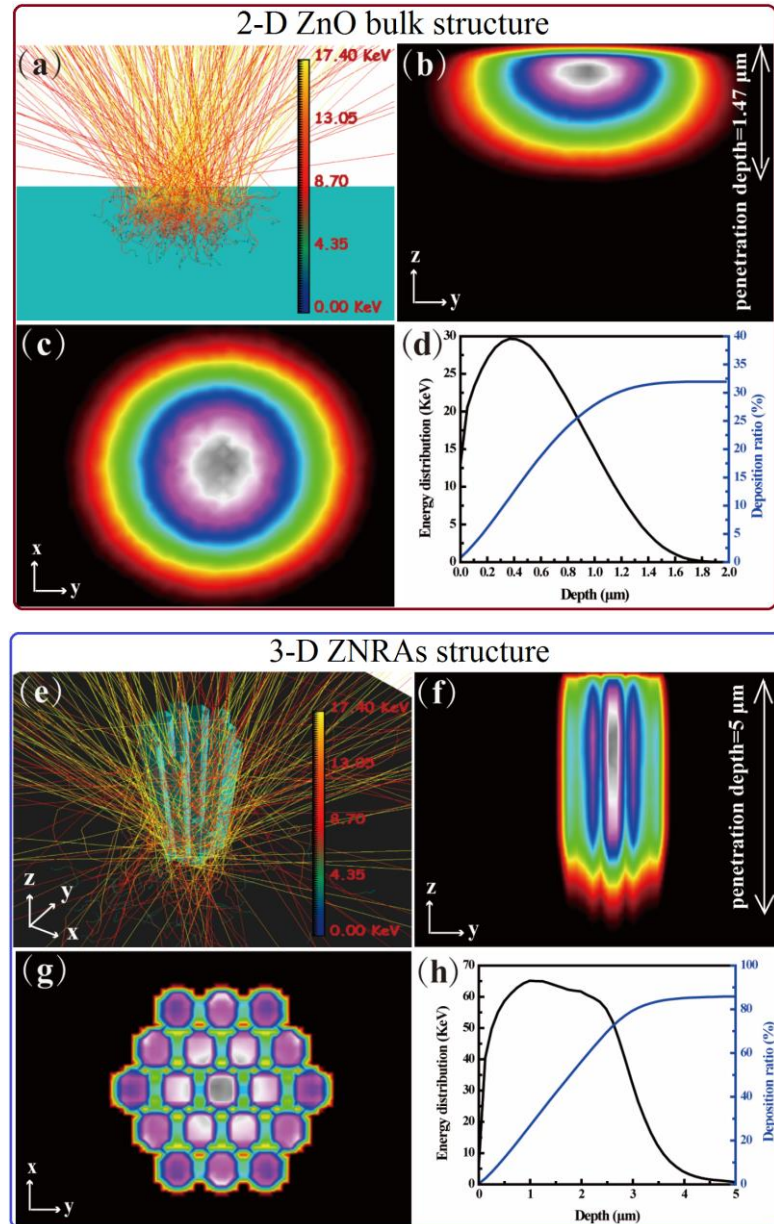


Fig. 2. (Color online) MC modeling and simulation of 2-D ZnO bulk structure and 3-D ZNRA structure under β irradiation. Scattering trajectories of β particles in (a) 2-D ZnO bulk structure and (e) 3-D ZNRA structure; energy deposition distributions of β particles in (b–c) 2-D ZnO bulk structure and (f–g) 3-D ZNRA structure on y – z plane and x – y plane; dependence of energy deposition density and deposition ratio on depth in (d) 2-D ZnO bulk structure and (h) 3-D ZNRA structure.

To qualitatively understand the interaction of incident β particles with ECSs, 2-D ZnO bulk and 3-D ZNRAs structures were modeled and simulated using the MC method. In this

mode, the ZnO thickness was set to 3 μm , and the diameter and length of the ZnO nanorods were set to 300 nm and 5 μm , respectively. An electron beam with a diameter of 1.8 μm and incident angle of 45° along the horizontal direction was used as the exciting source, and consisted of 1000 β particles with an average energy of 17.4 keV for the β particles of ^{63}Ni . The scattering trajectories and energy deposition distribution of the β particles in both structures were simulated using the CASINO software, as shown in Fig. 2. As shown in Fig. 2a, a fraction of the incident β particles was reflected from the surface of the bulk ZnO, which led to certain energy loss in the 2-D ZnO bulk structure. The energy deposition distributions of the incident β particles in the 2-D ZnO bulk exhibited an incident depth of approximately 1.47 μm on the y - z plane (Fig. 2b) and an interaction radius of 2.9 μm on the x - y plane (Fig. 2c). Fig. 2d shows the dependence of the energy deposition density and deposition ratio on the depth of the 2-D ZnO bulk structure. The maximum depth of energy deposition is approximately 1.47 μm , and the energy deposition ratio reached 32%. In contrast, the MC simulation yielded different results for the ZNRAs. The scattering behaviors of the β particles in the ZNRAs imply a higher structure trapping for the β particles compared with the 2-D ZnO bulk structure (Fig. 2e). Moreover, the simulation results for the energy deposition distribution in the ZNRAs (Fig. 2f and 2g) reveal that incident energy can be deposited in a very deep range along the length of the nanorods owing to the multiple scattering and absorption of β particles. This can be further verified by the simulation results for the dependence of the energy deposition density and energy deposition ratio on the depth in 3-D ZNRAs structures, as shown in Fig. 2h. Compared with the 2-D ZnO structure, the energy deposition depth in the 3-D ZNRAs structure could reach approximately 4.5 μm with an energy deposition rate of approximately 85%. This result indicates that the 3-D ZNRAs can harvest more β energy in the ECSs compared with the 2-D ZnO structures, which results in the higher ECE and P_{out} of BCs.

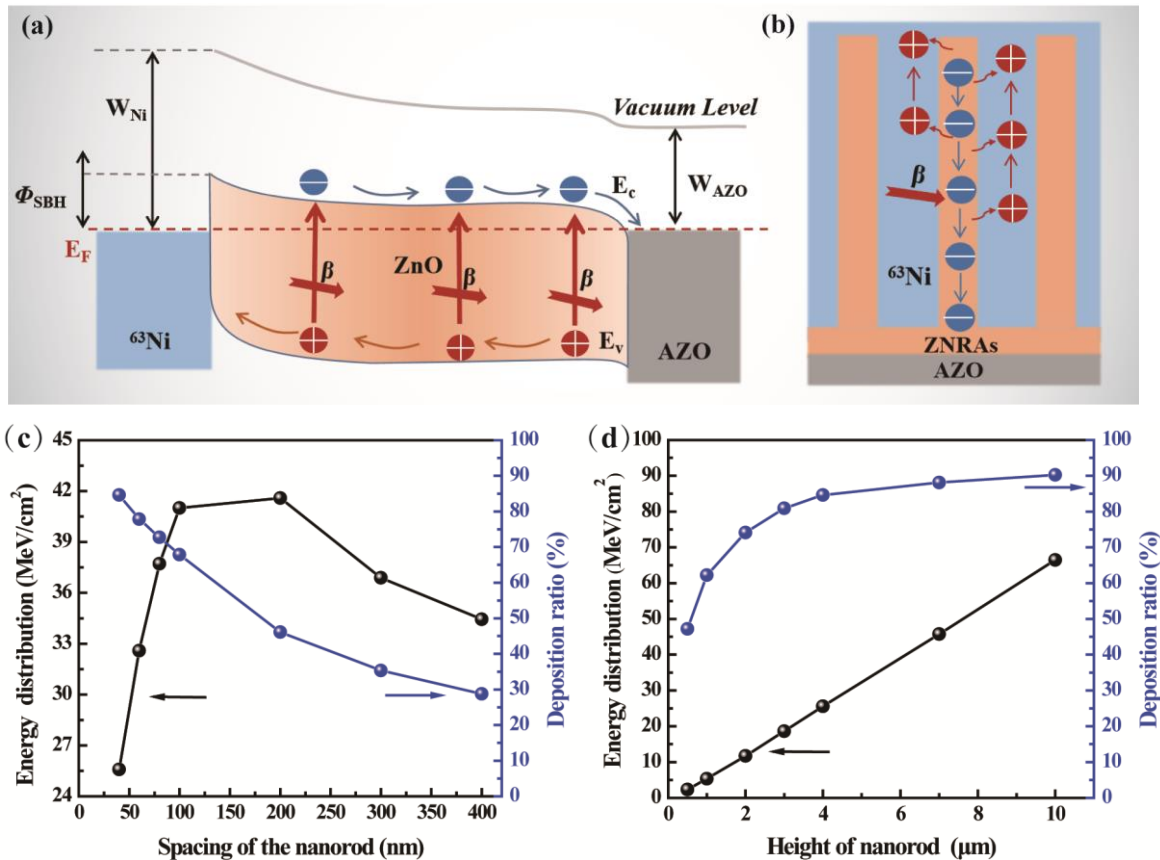


Fig. 3. (Color online) **(a)** Schematic energy band diagram of BC based on ^{63}Ni @ZNRAs and **(b)** transferring process of β excited carriers in ^{63}Ni @ZNRAs; **(c)** energy deposition and deposition ratio of incident β particles of devices based on ^{63}Ni @ZNRAs with different nanorod spacings; **(d)** energy deposition distribution and deposition ratio of incident β particles of devices based on ^{63}Ni @ZNRAs with different nanorod heights.

Figure 3 shows the working principle of the BCs based on ^{63}Ni @ZNRAs. A schematic energy band diagram is shown in Fig. 3a. An extended 3-D heterojunction of $^{63}\text{Ni}/\text{ZnO}$ is formed with a Schottky contact ($\Phi_{\text{SBH}} = W_m - \chi$) in the interface of $^{63}\text{Ni}/\text{ZnO}$ and an ohmic contact in the interface of AZO/ZnO. The β particles emitted from the ^{63}Ni source are incident on the ZnO lattice, where impact ionization results in the energy deposition and generation of electron-hole pairs (EHPs). The EHPs are separated by a built-in electric field in the depletion region of the $^{63}\text{Ni}/\text{ZnO}$ Schottky junction. In this process, electrons migrate from the conduction band (with energy level E_c) of ZnO to the AZO substrate, while holes are transferred from the valence band (with energy level E_v) of ZnO to the ^{63}Ni electrode [31]. Figure 3b shows the horizontal EHP separation and longitudinal carrier transport.

To simulate the β energy deposition in the ZNRAs with satisfactory accuracy, the MCNP software was used to establish the MC model of the ^{63}Ni @ZNRAs. This study used ^{63}Ni as an isotropic volumetric source integrated into the gap of the nanorods, and the number of incident β particles was set to 1×10^5 . The β energy deposition in the ZNRAs by radiation from the ^{63}Ni source was simulated using the actual spectrum of the emitted electrons. The energy deposition in the ZNRAs was calculated using the F8 pulse counting in the MCNP program, and the deposited energy could then be employed to calculate the actual current density using Eq. (2), as described in Sect. 2.2. The dependence of the energy deposition and deposition ratio of the incident β particles on the spacing and height of the nanorods is shown in Fig. 3c and 3d, respectively. As the spacing of the nanorods increased, the loading amount of ^{63}Ni increased, which led to an increase in the total β -emitting energy. However, the number of nanorods per unit area decreased as the spacing increased. Consequently, the energy deposition rate decreased. The trade-off reached a balance at the spacing of approximately 200 nm, where the maximum energy deposition was achieved (Fig. 3c). As the nanorod height increased, as shown in Fig. 3d, both the deposited energy and energy deposition ratio increased, and the energy deposition rate exhibited a trend of slow increase when the height exceeded 4 μm .

2.2. Quantitative modeling for BCs based on 3-D ZNRAs

A quantitative model should be established to accurately evaluate the performance of the BCs. Because the working principle of BCs is similar to that of solar cells, a conventional theoretical model of solar cells can be improved to establish a model of 3-D nanostructured BCs. As high-energy incident β particles on the ECSs, multiple electron-hole pairs (EHPs) are generated by the impact ionization of the β particles with the semiconductors. The EHPs are effectively separated and drawn as the theoretical maximum current density (I_{\max}), which can be calculated as follows [32]:

$$I_{\max} = eN_{\beta}(\overline{E_{\beta}}/\psi) \quad (1)$$

$$\psi = 2.8E_{\text{g}} + 0.5 \text{ eV} \quad (2)$$

where ψ is the ionization energy that generates an EHP; E_{g} is the bandgap of the

semiconductor; N_β is the β -emitting flux ($N_\beta = A \times 3.7 \times 10^7$); A is the activity (mCi) of the radioactive source; \bar{E}_β is the average energy of the β particles. The radiation-generated current (I_β) in the BCs is given as follows:

$$I_\beta = \varphi(1-\gamma)(1-\mu)(1-\sigma)QI_{\max} = QeE_s / \psi, \quad (3)$$

where γ is the reflection coefficient of the β particles from the semiconductor surface; μ is the interaction coefficient between the external medium (air or electrode) and incident β particles; σ is the self-absorption coefficient of the radioactive source, which is related to the thickness of the radioactive source; φ is the scattering angle coefficient of the radioactive source, which is the ratio of the number of incident particles on the semiconductor to the total number of emitted β particles. For 3-D ZNRAs, $\gamma = 0$, $\mu = 0$, $\varphi = 1$, e is the electron charge ($e = 1.6 \times 10^{-19} C$), and E_s is the β energy deposited in the semiconductors; Q is the collection efficiency, which is the ratio between the number of effective carriers for forming a current in the devices and the total number of carriers produced by the impact ionization of the incident β particles with the semiconductors. Here, Q is the collection efficiency of carriers in the space-charge region of the Schottky junction, which is approximately 100%; the collection efficiency of the carriers outside of the space charge region can be calculated as follows [33]:

$$Q = 1 - \tanh(d/L), \quad (4)$$

where d is the distance of the carrier moving to the boundary of the depletion region and L is the minority carrier diffusion length.

The width of the Schottky junction space-charge region can be calculated as follows [34]:

$$W = \sqrt{2\epsilon_0\epsilon_s(\Phi_{\text{SBH}} - V)/(eN_D)} \quad (5)$$

where ϵ_0 is the dielectric constant of the vacuum; ϵ_s is the relative dielectric constant of the semiconductor; N_D is the ZnO carrier concentration (approximately $2.1 \times 10^{15} \text{ cm}^{-3}$); Φ_{SBH} is the height of the Schottky barrier of Ni@ZnO ($\Phi_{\text{SBH}} = W_m - \chi = 0.8 \text{ eV}$), which is, the theoretical difference between the work function of Ni ($W_m = 5.15 \text{ eV}$) and the electron affinity energy of ZnO ($\chi = 4.35 \text{ eV}$).

From Eq. (5), the width of the depletion region of the Ni@ZnO Schottky barrier can be calculated as approximately $6.04 \times 10^{-1} \mu\text{m}$. Because the average diameter of the ZnO nanorods

(approximately 0.3 μm) grown using the hydrothermal method is smaller than the depletion region width, Q is approximately equal to 1 for BCs based on the ^{63}Ni @ZNAs structure.

Figure S1 shows the equivalent circuit model of the BCs (Supporting Information). The current density (I) delivered to the load resistor (R_L) at voltage V can be calculated as follows [35]:

$$I = I_\beta - \delta I_o [\exp(e(V + I\alpha R_s) / (nKT)) - 1] - (V + I\alpha R_s) / R_{sh} \quad (6)$$

$$\delta = S / S_o, \quad \alpha = (D_o H) / (D H_o), \quad (7)$$

where R_s and R_{sh} are the series and shunt resistances of the equivalent circuit of the BC, respectively. For the specific BC based on 3-D ZNAs that was prepared for the subsequent experiment, I_o , n , and R_s were extracted from its I - V curve measured under dark conditions, and the ideal R_{sh} was set to infinity. The greater height and smaller density of the nanorods will result in greater R_s . Considering that both I_o and R_s are variables related to the structural parameters of 3-D ZNAs, such as the area of the Schottky junction (S), nanorod array density (D), and nanorod height (H), two factors (δ and α) are combined with I_o and R_s in Eqs. (6–7). Thus, H_o and D_o are the structural parameters of the specific 3-D ZNAs structure.

The maximum short-circuit current (I_{sc}) of the BCs was calculated using Eq. (6). The open circuit voltage (V_{oc}) of the BCs can be calculated as follows:

$$V_{oc} = nkT \ln(I_{sc} / I_o + 1) / e, \quad (8)$$

where k is the Boltzmann constant ($k = 1.38 \times 10^{-23} \text{ J/K}$), T is the thermodynamic temperature at room temperature ($T = 300 \text{ K}$), I_o is the reverse saturation current, and n is an ideal factor.

The maximum output power (P_{max}), filling factor (FF), and energy conversion efficiency (η) can be expressed as follows [36]:

$$P_{max} = I_{sc} V_{oc} FF \quad (9)$$

$$FF = (I_{mp} V_{mp}) / (I_{sc} V_{oc}) \quad (10)$$

$$\eta = P_{max} / P_\beta \times 100\% = P_{max} / (e N_o \bar{E}_\beta) \times 100\% \quad (11)$$

where I_{mp} and V_{mp} are the current and voltage, respectively, corresponding to P_{max} ; P_β is the total power of the radioactive source; N_o is the total amount of β particles ($N_o = 3.7 \times 10^7 \times \Phi$,

where Φ is the activity of the radioactive source) emitted from the radioactive source.

2.3. Preparation of BCs based on 3-D ZNRAs nanostructure

The preparation process of the Ni-incorporated ZNRAs structure is shown in Fig. 4a. The ZNRAs were grown on Al-doped ZnO (AZO) conductive glass ($R_{\square} \leq 6 \Omega$, Nanotech, China) using a hydrothermal method [16]. First, the AZO conductive glass was cleaned using CH_3COCH_3 , ethanol ($\text{C}_2\text{H}_5\text{OH}$), and deionized water in an ultrasonic bath for 15 min. After drying, the specified electrode region in the AZO glass substrates was covered with high temperature tape, and the substrates were then transferred to a reactor with 10 ml of growth solution consisting of 0.05 M Zinc nitrate hexahydrate $[\text{Zn}(\text{NO}_3)_2 \cdot 6\text{H}_2\text{O}]$, 0.05 M hexamethylenetetramine ($(\text{CH}_2)_6\text{N}_4$, HMTA), 0.02 M polyetherimide (PEI), and deionized water. The temperature of the hydrothermal treatment was maintained at 95 °C for 4 h. Next, the samples were cleaned with deionized water and dried at 150 °C for 10 min. Finally, the samples were soaked in 10% concentration of hydrogen peroxide (H_2O_2) for 1 min for surface passivation, and then annealed in air at 400 °C for 2 h to obtain the ZNRAs [37]. Passivation treatment with H_2O_2 can reduce the surface defects of the ZnO nanorods, which favors the improvement of the Schottky diode characteristics. The incorporation of Ni into the ZNRAs was performed using a direct current (DC) magnetron sputtering technique. The vacuum chamber was evacuated to a pressure of 5×10^{-6} Pa, and Ar gas was then introduced into the chamber to reach the constant pressure of 0.6 Pa. Subsequently, Ni nanoparticles were deposited onto the ZNRAs using a DC power of 400 W at room temperature for 9 min. Fig. 4b shows a 3-D explosive diagram of the device based on the Ni-incorporated ZNRAs structure. To perform the I - V measurements, a planar Ni sheet was mechanically compressed onto the surface of the as-prepared samples to form a sandwich-type device with a Ni/Ni@ZNRAs/AZO/glass structure.

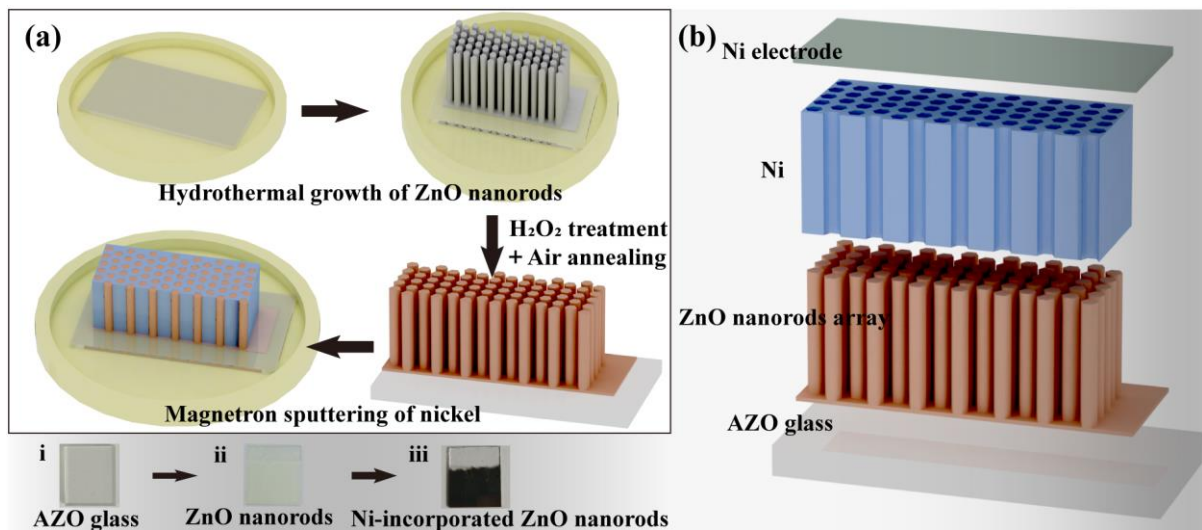


Fig. 4 (Color online) (a) Schematic illustration of preparation process flow of Ni-incorporated ZNRAs structure; (b) 3-D explosive diagram of device based on Ni-incorporated ZNRAs structure; (c) photographs of (i) AZO glass, (ii) ZNRAs/AZO glass, and (iii) Ni-incorporated ZNRAs/AZO/glass samples.

2.4. Material characterization and device measurements

Scanning electron microscopy (SEM, ZEISS microscope, Germany) and energy-dispersive X-ray spectroscopy (EDS) were used to analyze the morphology and chemical composition of the samples. The crystal structures were characterized by X-ray diffraction (XRD, D8 Advance, Bruker, Germany), and *I-V* measurements were performed in a Faraday cage using a Keithley Model 2450 source meter.

3. Results and discussion

3.1. Experimental results and discussion

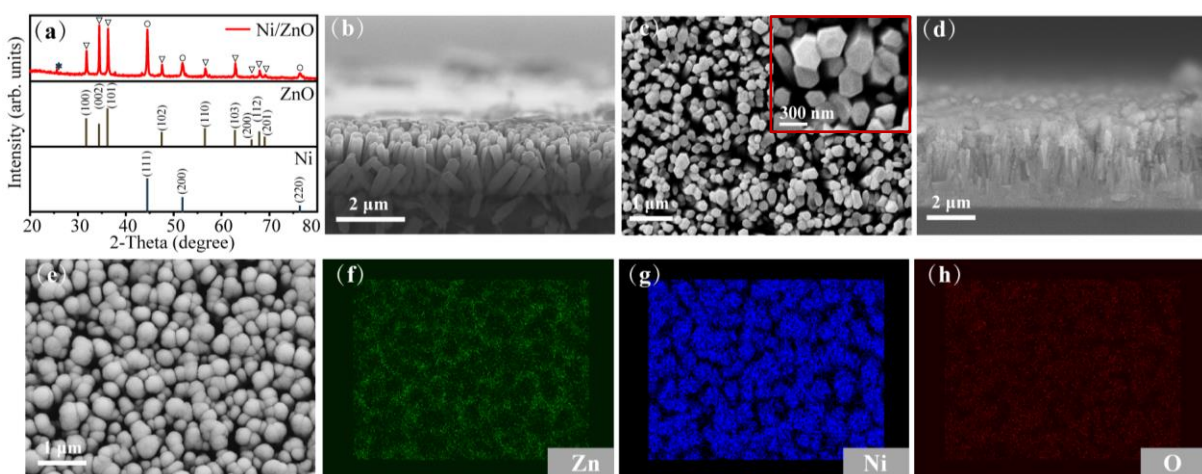


Fig. 5. (Color online) **(a)** XRD spectra of Ni@ZNRAs structure; **(b)** cross-section-view and **(c)** top-view SEM images of ZNRAs; **(d)** cross-section-view and **(e)** top-view SEM images of Ni@ZNRAs structure; **(f-h)** EDS mappings of Zn, Ni, and O.

The XRD pattern of the Ni@ZNRA structure is shown in Fig. 5a. All diffraction peaks can be indexed to the hexagonal structure of wurtzite ZnO (JCPDS card No. 36-1451) and cubic structure of Ni (JCPDS card No. 70-1849). The typical 2θ peaks at 34.4° and 36.3° are assigned to the (002) and (101) planes of ZnO, respectively. A new diffraction peak was not observed in the Ni@ZNRA structure, which indicates that the introduction of Ni did not change the crystal structure of the ZnO nanorods. The growth direction of the (002) crystal plane of ZnO is preferred to the c-axis orientation perpendicular to the substrate, as can be verified from the cross-sectional and top-view SEM images of the ZNRAs (Fig. 5b and Fig. 5c). The average diameter and height of the nanorods is 300 nm and 4 μm , respectively. The cross-section-view and top-view SEM images of the Ni@ZNRAs are shown in Fig. 5d and 5e, respectively. As can be clearly observed, Ni particles were uniformly filled into the gap between the ZnO nanorods and stacked to form a continuous Ni layer covering the surface of the ZNRAs. The SEM-EDS mappings show that Ni was adequately distributed on the surface of the ZnO nanorods, forming a core-shell structure (Fig. 5f-h).

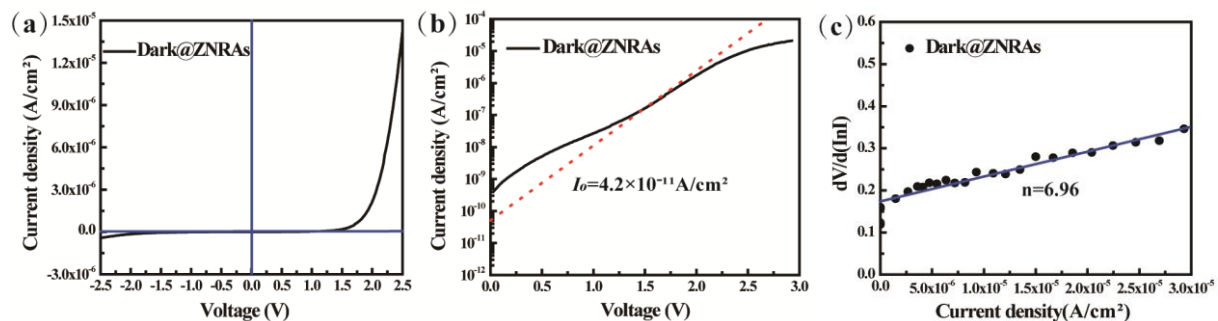


Fig. 6. Dark characteristics of devices based on Ni@ZNRAs/AZO structure: **(a)** linear-scale I - V curve in bias voltage range of -2.5–2.5 V; **(b)** logarithm-scale I - V curve in forward bias; **(c)** $dV/d(\ln I)$ - I curve.

Figure 6 shows the dark characteristics of the devices based on the Ni@ZNRAs/AZO structure. A typical I - V curve of the Schottky diode is shown in Fig. 6a, confirming the existence of the Ni/ZnO Schottky junction. The reverse saturation current of the device is $4.2 \times 10^{-11} \text{ A/cm}^2$, as determined by extrapolating the linear region of the logarithm-scale I - V

curve in the forward bias to zero bias voltage (Fig. 6b). The ideal factor n and series resistance R_s of the Schottky diode can be extracted from the dependence of $dV/d(\ln I)$ on the current (Fig. 6c) [38]. The extracted n and R_s are 6.96 and $248.45\ \Omega$, respectively. This ideal factor n is larger than 2, which indicates that the junction quality of Ni@ZNRAs is not perfect owing to the crystal defects or insufficient filling of Ni in the ZNRAs [39–40]. Fig. S2 (Supporting Information) shows the I - V curve of the devices based on the Ni@ZNRAs/AZO structure before H_2O_2 passivation and the calculated n value ($n = 11.2$). As can be seen, the n value before passivation is significantly larger compared with that after passivation, indicating that H_2O_2 passivation can significantly improve the diode quality. The presence of a large amount of interface defects in the ZnO nanorods may deteriorate the rectification characteristics of Schottky devices, leading to an increase in the reverse saturation current and ideal factor. In turn, the increase in reverse saturation current will decrease the open-circuit voltage, resulting in the decrease of output power, which can be calculated using Eq. 8. This indicates that H_2O_2 passivation improves the output power of the BCs. To evaluate the electrical performance of BCs based on the ^{63}Ni @ZNRAs structure, the above-mentioned parameter values of the Schottky diode are used in the quantitative model of BCs, as described in Sect. 2.2.

Table 1. Parameter values used in quantitative model of BCs.

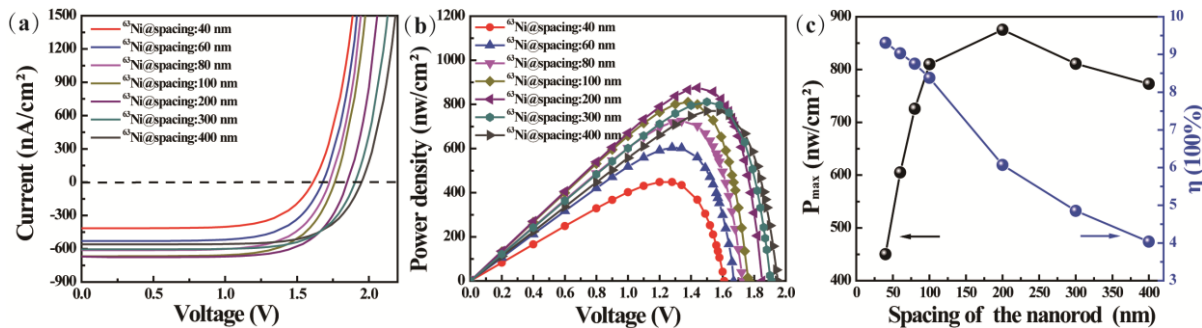
Parameters	Fixed value	Variable value
Reverse saturation current, I_0 (A/cm ²)	4.2×10^{-11}	–
Ideal factor, n	6.96	–
Series resistance, R_s (Ω)	248.45	–
Nanorod diameter, D (nm)	300	–
Nanorod height, H (μm)	–	0.5–10
Width of nanorod gap, W (nm)	–	40–400
Specific activity of ^{63}Ni , A_{sp} (Ci/g)	57	–
Average energy of ^{63}Ni , E_β (keV)	17.4	–
Mass density of ^{63}Ni , ρ (g/cm ³)	8.902	–

Table 1 lists the parameter values applied to the quantitative model of BCs. Notably,

these parameter values can be controlled and adjusted when growing ZNRAs using the hydrothermal method. Tao et al. [41] developed a combined lithography-assisted and hydrothermal growth approach to selectively control the spacing and size of ZNRAs on the ZnO seed layer. Sinem et al. [42] prepared ZNRAs with nanorod lengths greater than 60 μm by adjusting the contents of ammonium hydroxide and polyethyleneimine using a hydrothermal synthesis method. This means that the optimal values of nanorod parameters, such as the diameter, height, and density, can be prepared by adjusting process parameters such as the density of the ZnO seeds, concentration of the reactants, time and temperature of reactions, and pH values [43].

3.2. Simulated results and discussion

Using the fixed parameter values listed in Table 1 and an average nanorod height of 4 μm , the calculated I - V and P - V characteristics of BCs based on the ^{63}Ni @ ZNRAs structure with different nanorod spacings are as shown in Fig. 7a and Fig. 7b, respectively. By extracting P_{\max} from Fig. 7b and calculating the ECE according to the total activity of ^{63}Ni incorporated into the gap of the ZNRAs, the dependences of P_{\max} and ECE on the variable spacing of the nanorods can be obtained as shown in Fig. 7c. As can be seen, as the nanorod spacing increases, the activity of the ^{63}Ni incorporated into the gap of the nanorods also increases, resulting in the rapid increase of output power. However, as the nanorod spacing increases further, the nanorod density is reduced, which reduces the energy deposited on the ZNRAs and thus reduces the output power. Moreover, a maximum P_{out} at 875.4 nW/cm^2 corresponding to $I_{\text{sc}}=676.2$ nA/cm^2 and $V_{\text{oc}}=1.85$ V was achieved with $FF=0.699$ and $\eta=6.07\%$. In contrast, Figure 7c shows a monotonic decline in the ECE curve as the nanorod spacing increased. The ECE reached a maximum value of 9.3% when the spacing was set to 40 nm.



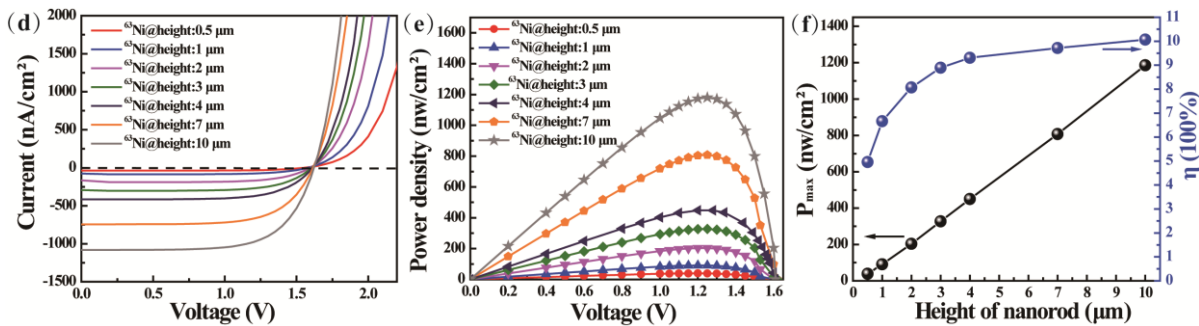


Fig. 7 (Color online) (a) I - V and (b) P - V characteristics of devices based on ^{63}Ni @ZNAs with different nanorod spacings; (c) dependences of P_{max} and ECE of devices based on ^{63}Ni @ZNAs on nanorod spacing; (d) I - V and (e) P - V characteristics of devices based on ^{63}Ni @ZNAs with different nanorod height; (f) dependences of P_{max} and ECE of devices based on ^{63}Ni @ZNAs on nanorod height.

The effects of the nanorod height on the ECE and P_{max} of the BCs were investigated under the optimal nanorod spacing. Fig. 7d and 7e shows the calculated I - V and P - V characteristics of the BCs based on the ^{63}Ni @ZNAs structure with different nanorod heights. As can be seen, I_{sc} increased with the nanorod height, while V_{oc} was kept at 1.62 V without any change. Fig. 7f shows the dependence of the P_{max} and ECE of the BCs on the nanorod height. The energy deposition ratio increased slowly when the nanorod height exceeded 4 μm (Fig. 3d), resulting in a slow increase in the saturation level of the energy conversion efficiency. As the nanorod height increased, the ECE tended toward the saturation value of approximately 10%, and the maximum P_{out} of 1185.9 nW/cm² was achieved when the height was 10 μm , corresponding to a loading amount of 114.37 mCi, I_{sc} of 1081.2 nA/cm², and FF of 0.673. Although long nanorods are beneficial for increasing the output power, it is difficult to fully deposit ^{63}Ni into a high-aspect-ratio ZNAs structure in practical operation. Hence, experimental investigation is required to determine the practical deposition depth of ^{63}Ni on the ZNAs.

To verify the advantages of 3-D nanostructures in enhancing the betavoltaic effect, a BC based on a 2-D ZnO bulk structure was investigated for comparison to the BCs based on a 3-D ZNAs structure, as shown in Fig. 1a. According to the MC simulation, the energy deposition depth of incident β particles in 2-D ZnO bulk is approximately 1.5 μm . Moreover, the dependence of the energy deposition and the deposition ratio of the incident β particles on the thickness of ^{63}Ni are shown in Fig. 8a. As the thickness of ^{63}Ni increases, the

self-absorption effect of the radiation source shields the β particles emitted from the deep location of the radiation source, resulting in deposition ratio reduction. As can be seen, the energy deposition tended to saturate when the thickness exceeded 1.5 μm . The dependences of P_{\max} and *ECE* of the BCs based on 2-D ZnO bulk on the thickness of ^{63}Ni were investigated, as shown in Fig. 8b. As the thickness of ^{63}Ni increased from 50 nm to 150 nm, the energy conversion efficiency increased from 4.05% to 4.69% owing to the deposited energy increase. As the thickness of ^{63}Ni increased further and exceeded 150 nm, the self-shielding effect of the radiation source became significant, which reduced the energy deposition ratio and thus reduced the energy conversion efficiency. It can be observed that P_{\max} tended toward saturation (approximately 135.2 nW/cm²) when the ^{63}Ni thickness reached 2 μm . Beyond this thickness, the self-shielding effect of the radioactive source limits the continued increase of output power. Moreover, the maximum *ECE* reached 4.69% when the ^{63}Ni thickness was 150 nm, as expressed by Eq. S8 (Supporting Information).

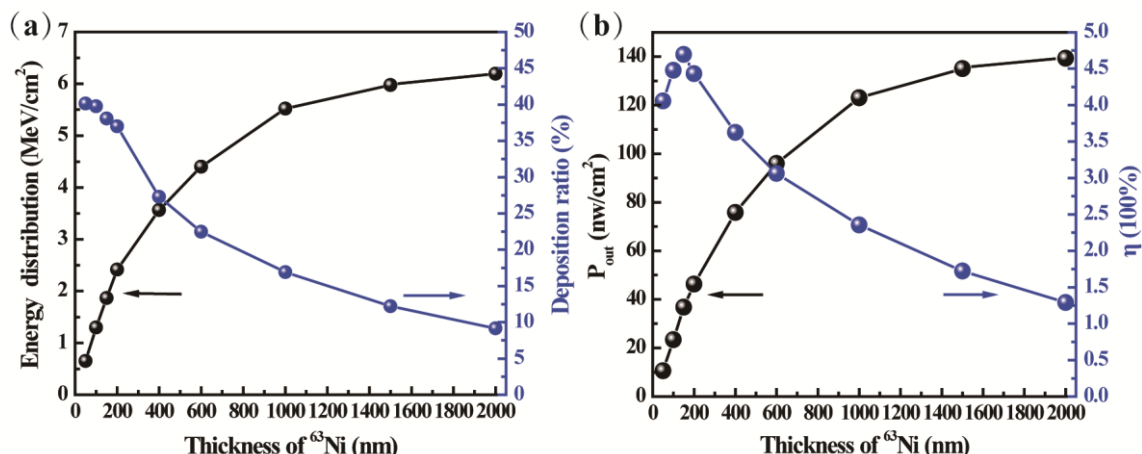


Fig. 8. (a) Energy deposition and deposition ratio of incident β particles of devices based on 2-D ZnO bulk with different ^{63}Ni thickness; (b) dependences of P_{\max} and *ECE* of BCs based on 2-D ZnO bulk on ^{63}Ni thickness.

The performance comparison between the BCs based on 3-D ZNRAs and those based on 2-D ZnO bulk is presented in Table 2. The BCs based on the 2-D ZnO film generated higher V_{oc} (1.87 V), which is attributed to the generation of lower reverse saturation current compared with the 3-D ZNRAs. Owing to the low utilization efficiency of the radioactive source, the β energy deposited in the semiconductor decreased dramatically, resulting in lower I_{sc} (28.1 nA/cm²) and P_{\max} (36.8 nW/cm²), which led to a low *ECE* of 4.69% compared with

the BCs based on the 3-D ZNRAs. According to the Shockley–Quaiser limit of photovoltaics [44], the efficiency cap of BCs is predicted to be as high as 13%, as can be calculated by $\eta = V_{oc}FF/\psi$. This means that 3-D ZNRAs with optimal structural design are significantly superior and can be used to prepare BCs close to their upper limits.

Table 2. Comparison of electrical parameters on 3-D and 2-D structured BCs.

Electrical parameters	Structures	
	3-D ZNRAs	2-D ZnO bulk
Maximum short circuit current density (nA/cm ²)	1081.2	28.1
Open circuit voltage (V)	1.62	1.87
Filling factor	0.673	0.701
Maximum output power (nW/cm ²)	1185.9	36.8
Energy conversion efficiency (%)	10.1	4.69

4. Conclusion

In summary, 3-D nanostructured WBGSSs are ideal candidates for increasing the *ECE* and output power of BCs. To evaluate and verify their advantages as a highly efficient β -energy-conversion structure, this study established a quantitative model for ⁶³Ni-powered BCs based on freestanding ZNRAs, and carried out MC modeling and simulation to obtain the deposited energy and maximum energy deposition depth. In the experiment, a BC based on a Ni-incorporated ZNRAs structure grown using the hydrothermal method was simulated to obtain the parameter values of the dark characteristics. By optimizing and simulating the BCs based on the 3-D ZNRAs structure and 2-D ZnO bulk structure, the performance of the ⁶³Ni-powered BCs based on both structures was evaluated using the quantitative model and experimental parameter values, respectively. In this study, the optimal nanorod spacing of the BCs based on 3-D ZNRAs was 40 nm and 200 nm for maximum energy conversion efficiency and maximum output power, respectively. The BCs based on 3-D ZNRAs achieved a maximum *ECE* of 10.1% and maximum output power of 1185.9 nW/cm², respectively. In

contrast, the values for the BCs based on the 2-D ZnO bulk are only 4.69% and approximately 135.2 nW/cm², respectively. The results confirm the significant superiority of the 3-D nanostructured WBGSSs in terms of increasing the *ECE* and output power of BCs.

Author contributions

All authors contributed to the study conception and design. Material preparation, data collection and analysis were performed by Zan Ding, Tong-Xin Jiang, Ren-Rong Zheng, Na Wang. The first draft of the manuscript was written by Zan Ding. Writing-review and editing of the manuscript were performed by Hai-Sheng San. Project administration and source support were performed by Li-Feng Zhang, Shi-Chao Liu, Xin Li, and Hai-Sheng San. All authors read and approved the final manuscript.

References

- [1] L.C. Olsen, P. Cabauy, B.J. Elkind, Betavoltaic power sources. *Phys. Today.* 65, 35-38 (2012). <https://doi.org/10.1063/PT.3.1820>
- [2] L.C. Olsen, Betavoltaic energy conversion. *Energy Conver.* 13, 117-124 (1973). [https://doi.org/10.1016/0013-7480\(73\)90010-7](https://doi.org/10.1016/0013-7480(73)90010-7)
- [3] C.L. Weaver, R.J. Schott, M A Prelas et al., Radiation resistant PIDE α cell using photon intermediate direct energy conversion and a 210 Po source. *Appl. Radiat. Isotopes.* 132, 110-115 (2018). <https://doi.org/10.1016/j.apradiso.2017.11.026>
- [4] M.G. Spencer, T. Alam, High power direct energy conversion by nuclear batteries. *Appl. Radiat. Isotopes.* 6, 031305 (2019). <https://doi.org/10.1063/1.5123163>
- [5] C.J. Eiting, V. Krishnamoorthy, S. Rodgers et al., Demonstration of a radiation resistant, high efficiency SiC betavoltaic. *Appl. Phys. Lett.* 88, 1-38 (2006). <https://doi.org/10.1063/1.2172411>
- [6] D.Y. Qiao, X.J. Chen, Y. Ren et al., A Micro Nuclear Battery Based on SiC Schottky Barrier Diode. *J. Microelectromech. S.* 20, 685-690 (2011). <https://doi.org/10.1109/JMEMS.2011.2127448>
- [7] A.A. Svintsov, A.A. Krasnov, M.A. Polikarpov et al., Betavoltaic battery performance: Comparison of modeling and experiment. *Appl. Radiat. Isotopes.* 137, 184-189 (2018). <https://doi.org/10.1016/j.apradiso.2018.04.010>
- [8] C. Munson, Q. Gaimard, K. Merghem et al., Modeling, Design, Fabrication and Experimentation of a GaN-based, ⁶³Ni Betavoltaic Battery. *J. Phys. D: Appl. Phys.* 51, 035101 (2017). <https://doi.org/10.1088/1361-6463/aa9e41>
- [9] S. Butera, M.D.C. Whitaker, A.B. Krysa et al., Investigation of a temperature tolerant InGaP (GaInP) converter layer for a ⁶³Ni betavoltaic cell. *J. Phys. D: Appl. Phys.* 50, 345101 (2017). <https://doi.org/10.1088/1361-6463/aa7bc5>
- [10] J. Dixon, A. Rajan, S. Bohlemann et al., Evaluation of a silicon 90Sr betavoltaic power source. *Sci. Rep.* 6, 38182 (2016). <https://doi.org/10.1038/srep38182>
- [11] W. Sun, N.P. Kherani, K.D. Hirschman et al., A three-dimensional porous silicon p-n diode for betavoltaics and photovoltaics. *Adv. Mater.* 17, 1230-1233 (2005). <https://doi.org/10.1002/adma.200401723>
- [12] J.W. Murphy, L.F. Voss, C.D. Frye et al., Design considerations for three-dimensional

betavoltaics. *Aip. Adv.* 9, 065208 (2019). <https://doi.org/10.1063/1.5097775>

[13] Y. Ma, N. Wang, J. Chen et al., Betavoltaic enhancement using defect-engineered TiO_2 nanotube arrays through electrochemical reduction in organic electrolytes. *Acs Appl. Mater. Inter.* 10, 22174-22181 (2018). <https://doi.org/10.1021/acsami.8b05151>

[14] C.S. Chen, N. Wang, P. Zhou et al., Electrochemically reduced graphene oxide on well-aligned titanium dioxide nanotube arrays for betavoltaic enhancement. *Acs Appl. Mater. Inter.* 8, 24638-24644 (2016). <https://doi.org/10.1021/acsami.6b08112>

[15] Q. Zhang, R.B. Chen, H.S. San et al., Betavoltaic effect in titanium dioxide nanotube arrays under build-in potential difference. *J. Power Sources.* 282, 529-533 (2015) <https://doi.org/10.1016/j.jpowsour.2015.02.094>

[16] C.S. Chen, J. Chen, Z. Wang et al., Free-standing ZnO nanorod arrays modified with single-walled carbon nanotubes for betavoltaics and photovoltaics. *J. Mater. Sci. Technol.* 19, 48-57 (2020). <https://doi.org/10.1016/j.jmst.2020.03.040>

[17] N. Wang, Y. Ma, J. Chen, C.S. Chen et al., Defect-induced betavoltaic enhancement in black titania nanotube arrays. *Nanoscale.* 10, 13028-13036 (2018). <https://doi.org/10.1039/c8nr02824a>

[18] N. Wang, R.R. Zheng, T.X. Chi et al., Betavoltaic-powered electrochemical cells using TiO_2 nanotube arrays incorporated with carbon nanotubes. *Compos Part B-Eng.* 239, 109952 (2022). <https://doi.org/10.1016/j.compositesb.2022.109952>

[19] R.R. Zheng, Z. Wang, C.Q. Zhang et al., Photocatalytic enhancement using defect-engineered black mesoporous $\text{TiO}_2/\text{CeO}_2$ nanocomposite aerogel. *Compos. Part B-Eng.* 222, 109037 (2021). <https://doi.org/10.1016/j.compositesb.2021.109037>

[20] Quintana, Maria, Edvinsson, Tomas et al. Comparison of Dye-Sensitized ZnO and TiO_2 Solar Cells: Studies of Charge Transport and Carrier Lifetime. *J. Phys. Chem. C* 111, 1035-1041 (2007). <https://doi.org/10.1021/jp065948f>

[21] M. Wang, J. Bai, FL. Formal et al., Solid-State Dye-Sensitized Solar Cells using Ordered TiO_2 Nanorods on Transparent Conductive Oxide as Photoanodes. *J. Phys. Chem. C* 116, 3266-3273 (2012). <https://doi.org/10.1021/jp209130x>

[22] H. Zhang, AV. Babichev, G. Jacopin et al., Characterization and modeling of a ZnO nanowire ultraviolet photodetector with graphene transparent contact. *J. Appl. Phys.* 114, 7433-7473 (2013). <https://doi.org/10.1063/1.4854455>

[23] X. Wang, Y. Han, J. Zhang et al., The design of a direct charge nuclear battery with high energy conversion efficiency. *Appl. Radiat. Isotopes.* 148, 147-151 (2019). <https://doi.org/10.1016/j.apradiso.2019.03.040>

[24] M. Wu, J. Zhang, Design and simulation of high conversion efficiency betavoltaic battery based on a stacked multilayer structure. *AIP Adv.* 9, 075124 (2019). <https://doi.org/10.1063/1.5094826>

[25] X.Y. Li, J.B. Lu, Y.M. Liu et al., Exploratory study of betavoltaic battery using ZnO as the energy converting material. *Nucl. Sci. Tech.* 30, 4 (2019). <https://doi.org/10.1007/s41365-019-0577-3>

[26] Y.J. Yoon, J.S. Lee, I.M Kang et al., Design and optimization of GaN-based betavoltaic cell for enhanced output power density. *Int. J. Energ. Res.* 45, 799-806 (2021). <https://doi.org/10.1002/er.5909>

[27] Z. Song, C. Zhao, F. Liao et al., Perovskite-Betavoltaic Cells, A Novel Application of Organic-Inorganic Hybrid Halide Perovskites. *Acs. Appl. Mater. Inter.* 11, 32969-32977 (2019). <https://doi.org/10.1021/acsami.9b09952>

- [28] Y.P. Liu, X.B. Tang, Z.H. Xu et al., Influences of planar source thickness on betavoltaics with different semiconductors. *J. Radioanal Nucl. Ch.* 304, 517-525 (2015). <https://doi.org/10.1007/s10967-014-3879-2>
- [29] X.Y. Li, J.B. Lu, R.Z. Zheng et al., Comparison of time-related electrical properties of PN junctions and Schottky diodes for ZnO-based betavoltaic batteries. *Nucl. Sci. Tech.* 31, 18 (2020). <https://doi.org/10.1007/s41365-020-0723-y>
- [30] H. Demers, N.P. Demers, A.R. Couture et al., Three-dimensional electron microscopy simulation with the CASINO Monte Carlo software. *Scanning.* 33, 135-146 (2011). <https://doi.org/10.1002/sca.20262>
- [31] M. Chen, L.F. Hu, J.X. Xu et al., ZnO hollow-sphere nanofilm-based high-performance and low-cost photodetector. *Small.* 7, 2449-2453 (2011). <https://doi.org/10.1002/smll.201100694>
- [32] X.B. Tang, Y.P. Liu, D. Ding et al., Optimization design of GaN betavoltaic microbattery. *Sci. China Tech. Sci.* 55, 659–664 (2012). <https://doi.org/10.1007/s11431-011-4739-8>.
- [33] X.B. Tang, D. Ding, Y.P. Liu et al., Optimization design and analysis of Si-⁶³Ni betavoltaic battery. *Sci. China Technol. Sc.* 55, 990-996 (2012). <https://doi.org/10.1007/s11431-012-4752-6>
- [34] D. Y. Qiao, X. J. Chen, Y. Ren et al., A micro nuclear battery based on SiC schottky barrier diode. *J. Microelectromech. S.* 20, 685-690 (2011). <https://doi.org/10.1109/JMEMS.2011.2127448>
- [35] H. Gao, S.Z. Luo, H.M. Zhang et al., Demonstration, radiation tolerance and design on a betavoltaic micropower. *Energy.* 51, 116-122 (2013). <https://doi.org/10.1016/j.energy.2012.12.042>
- [36] C. Zhao, L. Lei, F. Liao et al., Efficiency prediction of planar betavoltaic batteries basing on precise modeling of semiconductor units. *Appl. Phys. Lett.* 117, 263901 (2020). <https://doi.org/10.1063/5.0033052>
- [37] S.H. Yang, Y.J. Lin, H.C. Chang et al., Effects of H₂O₂ treatment on the optical and structural properties of ZnO nanorods and the electrical properties of conductive polymer/ZnO-nanorod array diodes. *Thin Solid Films.* 545, 476-479 (2013). <https://doi.org/10.1016/j.tsf.2013.08.063>
- [38] S.K. Cheung, N.W. Cheung, Extraction of schottky diode parameters from forward current-voltage characteristics. *Appl. Phys. Lett.* 49, 85-87 (1986). <https://doi.org/10.1063/1.97359>
- [39] S. Mridha, D. Basak, ZnO/polyaniline based inorganic/organic hybrid structure: Electrical and photoconductivity properties. *Appl. Phys. Lett.* 92, 42 (2008). <https://doi.org/10.1063/1.2898399>
- [40] Z. Yuan, Low-temperature growth of well-aligned ZnO nanorod arrays by chemical bath deposition for schottky diode application. *J. Electron. Mater.* 44, 1187-1191 (2015). <https://doi.org/10.1007/s11664-015-3661-4>
- [41] Y.L. Tao, M. Fu, A.L. Zhao et al., The effect of seed layer on morphology of ZnO nanorod arrays grown by hydrothermal method. *J. Alloy Compd.* 489, 99-102 (2010). <https://doi.org/10.1016/j.jallcom.2009.09.020>
- [42] S.V. Kurudirek, K.C. Pradel, C.J. Summers, Low-temperature hydrothermally grown 100 μ m vertically well-aligned ultralong and ultradense ZnO nanorod arrays with improved PL property. *J. Alloy Compd.* 702, 700-709 (2017). <https://doi.org/10.1016/j.jallcom.2017.01.273>

[43] M. Fang, Z.W. Liu, Controllable size and photoluminescence of ZnO nanorod arrays on Si substrate prepared by microwave-assisted hydrothermal method. *Ceram. Int.* 43, 6955-6962 (2017). <https://doi.org/10.1016/j.ceramint.2017.02.119>

[44] W. Shockley, H.J. Queisser, Detailed balance limit of efficiency of p-n junction solar cells. *J. Appl. Phys.* 32, 510-519 (1961). <https://doi.org/10.1063/1.1736034>